Polarization-sensitive cathodoluminescence Fourier microscopy

Toon Coenen[*] **and Albert Polman**
Center for Nanophotonics, FOM Institute AMOLF,
Science Park 104, 1098 XG, Amsterdam, The Netherlands
[*]*coenen@amolf.nl*

Abstract: Determining the emission polarization properties of sub-wavelength structures like optical nanoantennas, nanocavities and photonic crystals is important to understand their physical properties and to optimize their use in applications. Recently we have shown that angle-resolved cathodoluminescence imaging spectroscopy (ARCIS), which uses a 30 keV electron beam as an excitation source, is a useful technique to study the far-field properties of such structures. Here we extend the technique with polarization-sensitive angular detection. As proof-of-principle, we experimentally probe the emission polarization properties of three orthogonal dipolar emitters of which the polarization is well-known and find excellent agreement between experiment and theory. We access these dipole orientations by exciting an unstructured gold surface and a ridge nanoantenna with an in-plane dipolar plasmon resonance. The light emission is collected with an aluminum half paraboloid mirror. We show how to take the effect of the paraboloid mirror on the emission polarization into account and how to predict the polarization-filtered pattern if the emission polarization is known. Furthermore, we calculate that by introducing a slit in the beam path the polarization contrast in cathodoluminescence spectroscopy can be strongly enhanced. Finally, we reconstruct the emission polarization from the experimental data and show that from these field patterns we can infer the orientation of the induced dipole moment. The ability to measure the emission polarization, in combination with the sensitivity to the local density of optical states, broad spectral range and high excitation resolution, can be employed to study photonic nanostructures in great detail.

OCIS codes: (070.0070) Fourier optics and signal processing; (250.1500) Cathodoluminescence.

References and links

1. J. D. Jackson, "*Classical Electrodynamics*" (John Wiley and Sons, Hoboken, 1999).
2. L. Novotny and B. Hecht, *Principles of Nano-Optics* (Cambridge University Press, New York, 2006), 251–362.
3. N. J. Halas, S. Lal, W. Chang, S. Link, and P. Nordlander, "Plasmons in strongly coupled metallic nanostructures," Chem. Rev. **111 (6),** 3913–3961 (2011).
4. L. Cao, J. S. White, J. Park, J. A. Schuller, B. M. Clemens, and M. L. Brongersma, "Engineering light absorption in semiconductor nanowire devices," Nat. Mater. **8,** 643–647 (2009).
5. A. W. Snyder and J. D. Love, *Optical Waveguide Theory* (Chapman and Hall, London, 1983).

6. K. J. Klein Koerkamp, S. Enoch, F. B. Segerink, N. F. van Hulst, and L. Kuipers, "Strong influence of hole shape on extraordinary transmission through periodic arrays of subwavelength holes," Phys. Rev. Lett. **92,** 183901 (2004).

7. O. L. Muskens, V. Giannini, J. A. Sánchez-Gil, and J. Gómez Rivas, "Optical scattering resonances of single and coupled dimer plasmonic nanoantennas," Opt. Express **15,** 17736–17746 (2007).

8. M. A. Lieb, J. M. Zavislan, and L. Novotny, "Single-molecule orientations determined by direct emission pattern imaging," J. Opt. Soc. Am. B **21,** 1210–1215 (2004).

9. I. Sersic, C. Tuambilangana, and A. F. Koenderink, "Fourier microscopy of single plasmonic scatterers," New. J. Phys. **13,** 083019 (2011).

10. A. G. Curto, G. Volpe, T. H. Taminiau, M. P. Kreuzer, R. Quidant, and N. F. van Hulst, "Unidirectional emission of a quantum dot coupled to a nanoantenna," Science **329,** 930–933 (2010).

11. K. G. Lee, X. Chen, H. Eghlidi, P. Kukura, R. Lettow, A. Renn, V. Sandoghdar, and S. Götzinger, "A planar dielectric antenna for directional single-photon emission and near-unity collection efficiency," Nat. Photonics **5,** 166–169 (2011).

12. T. Coenen, E. J. R. Vesseur, A. Polman, and A. F. Koenderink, "Directional emission from plasmonic Yagi Uda antennas probed by angle-resolved cathodoluminescence spectroscopy," Nano Lett. **11,** 3779–3784 (2011).

13. T. Coenen, E. J. R. Vesseur, and A. Polman, "Angle-resolved cathodoluminescence spectroscopy," Appl. Phys. Lett. **99,** 143103 (2011).

14. E. J. R. Vesseur and A. Polman, "Plasmonic whispering gallery cavities as optical antennas," Nano Lett. **11,** 5524–5530 (2011).

15. T. Coenen, E. J. R. Vesseur, and A. Polman, "Deep subwavelength spatial characterization of angular emission from single-crystal Au plasmonic ridge nanoantennas," ACS Nano **6,** 1742–1750 (2012).

16. M. Kuttge, E. J. R. Vesseur, A. F. Koenderink, H. J. Lezec, H. A. Atwater, F. J. García de Abajo, and A. Polman, "Local density of states, spectrum, and far-field interference of surface plasmon polaritons probed by cathodoluminescence," Phys. Rev. B **79,** 113405 (2009).

17. F. J. García de Abajo, "Optical excitations in electron microscopy," Rev. Mod. Phys **82,** 209–275 (2010).

18. P. B. Jonhson and R. W. Christy, "Optical constants of noble metals," Phys. Rev. B **6,** 4370–4379 (1972).

19. K. Takeuchi and N. Yamamoto, "Visualization of surface plasmon polariton waves in two-dimensional plasmonic crystal by cathodoluminescence," Opt. Express **19,** 12365–12374 (2011).

20. H. T. Lin, D. H. Rich, A. Konkar, P. Chen, and A. Madhukar, "Carrier relaxation and recombination in GaAs/AlGaAs quantum heterostructures and nanostructures probed with time-resolved cathodoluminescence," J. Appl. Phys. **81,** 3186–3195 (1997).

21. D. H. Rich, Y. Tang, A. Konkar, P. Chen, and A. Madhukar, "Polarized cathodoluminescence study of selectively grown self-assembled InAs/GaAs quantum dots," J. Appl. Phys. **84,** 6337–6344 (1998).

22. N. Yamamoto, S. Bhunia, and Y. Watanabe, "Polarized cathodoluminescence study of InP nanowire by transmission electron microscopy," Appl. Phys. Lett. **88,** 154106 (2006).

23. J. B. Lassiter, H. Sobhani, M. W. Knight, W. S. Mielczarek, P. Nordlander, and N. J. Halas, "Designing and deconstructing the Fano lineshape in plasmonic nanoclusters," Nano Lett. **12,** 1058–1062 (2012).

1. Introduction

The degree of coupling between light and matter strongly depends on the polarization of the incoming electromagnetic field. For instance, a point-dipole emitter like a dye-molecule, nitrogen vacancy center or quantum dot is most efficiently driven when the electric field of the light wave is aligned with its electric dipole axis [1, 2]. Moreover, in optically active (bio)molecules the handedness of the light can also influence the coupling strength. The ability to manipulate and probe the polarization state of light is key in many applications including lasers, flat screen televisions and video projectors. Also in the field of nanophotonics polarization plays an important role. The excitation efficiency of a localized surface plasmon resonance (LSPR) [3], Mie resonance [4], or guided mode [5] often is polarization dependent. For instance, one can access two orthogonally oriented dipole resonances in a rectangular hole surrounded by metal or in a metallic nanorod by choosing the incoming polarization either along or transverse to the long axis of the structure [6, 7]. Vice versa, when such a resonance is driven by an incident light wave or localized source, the far-field emission can also be strongly polarized in a way that is characteristic for the charge distribution associated with that resonance. Measuring the emission polarization can be used to deduce in which direction a structure is polarized.

In optical microscopy, the far-field emission pattern of molecules [8], nanoantennas [9] and

coupled systems (where a localized emitter is coupled to an antenna) [10, 11] can be obtained by imaging the back focal plane of the microscope objective (Fourier microscopy). When performing Fourier microscopy on nanoantennas fed by fluorescent probes like quantum dots or dye molecules, the pump light can be separated from the fluorescence by using a color filter or dichroic mirror because the fluorescence is Stokes-shifted from the pump light. The bandwidth of these probes is limited however, so as an alternative, one can also measure optical scattering directly to study the scattering properties of the antenna. Although this method potentially gives broadband information on the scattering properties of a structure it is not possible to selectively separate the scattering from the pump light by means of a color filter. As a result the background signal from the excitation beam usually is relatively strong in such measurements, making it more difficult to see the angular distribution from the scattering object. It has been shown recently by Sersic *et al.* that this can be solved by using a dark-field excitation configuration like a prism (total internal reflection (TIR) mode) [9].

Recently, we have demonstrated that angle-resolved cathodoluminescence (CL) imaging spectroscopy (ARCIS) is a good alternative technique for studying the far-field emission properties of nanoantennas [12-15]. In CL spectroscopy an energetic electron beam, focused into a nanoscale spot, is used as broadband excitation source. Because of its high excitation resolution (∼10 nm) one can efficiently excite a single structure with a relatively low background signal, essentially making it a dark-field technique as well, where the optical scattering from a single antenna dominates the Fourier image. However, up until now it has not been possible to obtain the polarization of the emission for different emission angles. In this article we
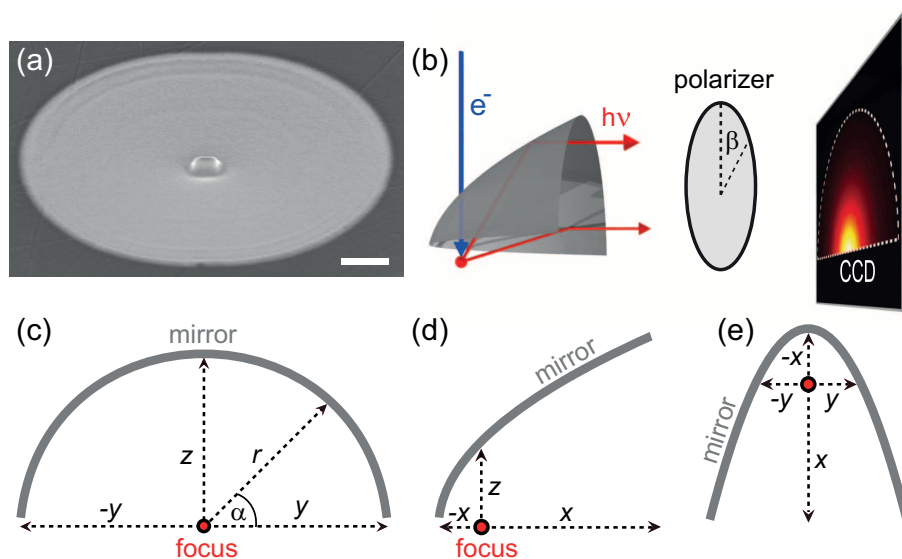

Fig. 1. (a) Scanning electron micrograph of a 300 nm long ridge antenna taken at a 52° inclination of the microscope stage. The scale bar represents 500 nm (b) Schematic overview of the experimental setup. The electron beam (blue arrow) excites the sample generating CL (red arrows) which is collected by the paraboloid mirror and converted into a parallel beam. The beam goes through a linear polarizer set at an angle β and is projected onto a 2D CCD array. $\beta = 0°$ corresponds to alignment of the polarizer with the z-direction. (c) Front view, (d) side view, and (c) top view perspective of the paraboloid mirror showing the coordinate system that is used. For clarity only the mirror contours are shown.

show how to deduce the emission polarization when using angle-resolved CL imaging, thereby adding an extra dimension to the technique. As proof-of-principle, we experimentally probe the emission polarization properties of three orthogonal dipolar emitters of which the polarization is well-known and find excellent agreement between experiment and theory.

2. Sample and experimental setup

In this experiment we use a Czochralski grown single-crystal gold substrate with a polished surface. We study CL emission originating from an unstructured part of the sample as well as from a 300 nm long, 120 wide, and 130 nm high plasmonic ridge nanoantenna (for a more detailed description see ref. [15]), fabricated using focused-ion-beam (FIB) milling by inversely patterning the gold surface. A scanning electron micrograph of the structure is shown in Fig. 1(a). We use a 30 keV electron beam (1 nA beam current) from a scanning electron microscope (SEM) as a broadband nanoscale excitation source. The resulting CL emission is collected using an aluminum half-paraboloid mirror (effective NA of 1.46π sr) and directed towards a 2D 1024x1024 pixel imaging camera which measures the intensity profile of the beam (see Fig. 1(b)). From this profile the angular intensity distribution of the emission can be deduced [12, 13]. We place a linear polarizer fixed in a rotation mount in between the camera and the mirror, allowing detection of the angular CL emission pattern for different polarizer angles β. For wavelength selectivity we use 40 nm band pass color filters, that are placed in the beam path. For further use in the article we define a cartesian coordinate system where the x-dimension is aligned with the optical axis of the mirror, the z-dimension is parallel to the incoming electron beam and the y-dimension is transverse to the optical mirror axis. Figures 1(c-e) illustrate how the coordinate system is oriented with respect to the mirror.

3. Measuring and calculating polarization-filtered angular patterns

When an electron passes through an interface between two dielectric environments, it induces a broadband transient dipole on the surface which radiates into the far field (transition radiation (TR)) [16, 17]. This dipole moment is oriented vertically with respect to the interface (z-direction, parallel to the electron beam) and the corresponding angular emission pattern has a characteristic toroidal 'doughnut' shape [13]. The toroid is bent upwards due to the reflective metal substrate. Figure 2(a) shows the calculated emission intensity for TR as function of zenithal angle θ and azimuthal angle ϕ. All radiation patterns shown in this article are normalized to 1. The emission pattern was calculated for a free-space wavelength (λ_0) of 650 nm using the expressions for TR-emission [17] and tabulated permittivity values for the gold substrate [18]. The ridge antenna exhibits an in-plane dipolar resonance aligned with its long axis (in the xy-plane parallel to the surface) at λ_0=650 nm, which is most efficiently excited by the electron beam at the extremities of the ridge (see Figs. 2(b,e) in Ref. [15]). Figure 2(b) shows the emission pattern for an in-plane dipole calculated using asympotic far-field expressions for a point dipole above a substrate [2]. In this case we have placed the dipole 65 nm (half of the antenna height) above the gold surface. The pattern now shows one emission lobe pointing towards the normal. By rotating the SEM sample stage with respect to the mirror in the xy-plane we can probe the emission polarization response for x-and y-oriented dipoles. Thus, by using both the unstructured substrate and ridge we have access to three orthogonal dipole orientations with known emission polarization which we can use to test the polarization sensitivity of our experimental setup.

Figures 2(c,d) show cross cuts through (a) and (b) along the blue dashed line ($\phi = 90 - 270°$) yielding emission intensity as function of θ (blue solid curves) in which we have indicated the polarization direction $\hat{\mathbf{e}}$ (red arrows) for different emission directions $\hat{\mathbf{d}}$. The electric field orientation for (c) corresponds to that of a vertically oriented point dipole source [2] and to an
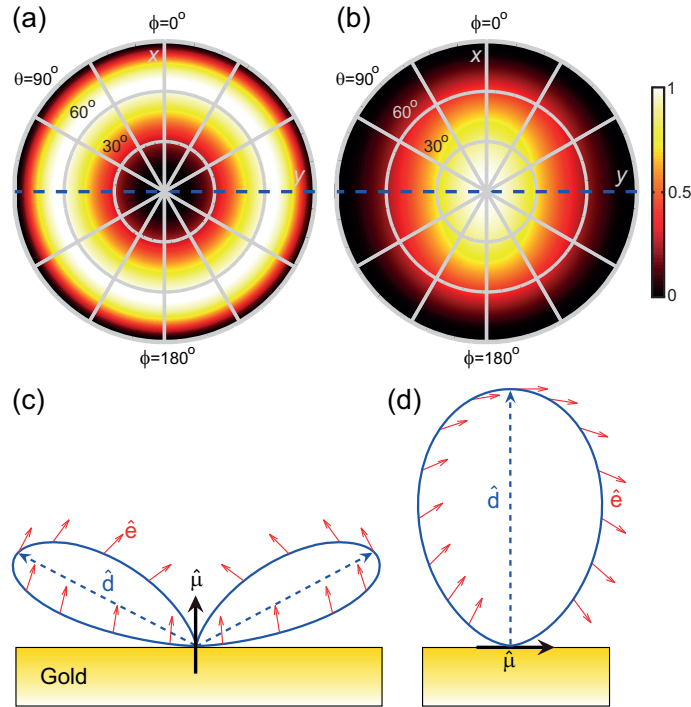
Fig. 2. (a) Caluclated normalized cathodoluminescence emission intensity as function of zenithal angle θ and azimuthal angle ϕ for TR on a gold substrate which is similar to the pattern for a vertically oriented dipole $\hat{\mu}$ (black arrow). (b) Calculated angular pattern for an in-plane point dipole like the ridge antenna, aligned along y. (c,d) Cross cuts through (a) and (b) along the blue dashed lines showing the angular patterns as function of θ. For each emission direction $\hat{d}$ there is a corresponding electric field orientation $\hat{e}$ which is indicated by the red arrows for a selection of emission directions.

in-plane point dipole for (d). It is clear that the vertical dipole is radially polarized (p-polarized) whereas for the in-plane dipole the emission polarization is aligned with the dipole moment

In optical Fourier microscopy light is usually collected with a high quality microscope objective. Such an objective converts the light originating from a point source at the focal point to a plane wave propagating in the z-direction. Assuming that we have a 'perfect' objective (no aberrations and perfect transmission), calculating its effect on the dipole emission polarization is quite straightforward since all the electric field components are projected onto the xy-plane, transverse to the propagation direction. The resulting polarization-filtered angular pattern is a convolution of the far-field pattern and the polarization filtering after light collection. Figure 3 shows the angular emission intensity collected with a NA=0.96 (same acceptance angle as the paraboloid) objective for z-and y-dipole orientations, respectively, when the polarizer is aligned with the x-or y-axis. The black ring around the pattern corresponds to grazing angles that are not collected by the objective. For a z-dipole, the part of the emission toroid where the field is (partly) aligned with the polarizer is transmitted. Due to its azimuthally symmetric field distribution this pattern rotates along with the polarizer. For the y-dipole the dipole emission pattern is relatively well-preserved when the polarizer is aligned with the dipole-axis. However, for the cross-polarization the pattern is strongly altered and shows four off-normal lobes. For a x-dipole the result is the same but rotated by 90°.
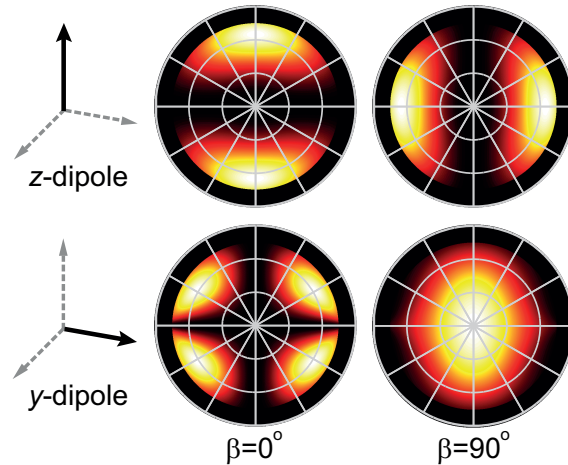
Fig. 3. Calculated radiation patterns for a *z*-and *y*-dipole collected with a 'perfect' optical microscope objective (NA=0.96).

To study the emission polarization for the three dipole orientations in our experimental setup, we excite the bare gold substrate and the ridge antenna and collect a polarization-filtered CCD-image for 120 seconds at λ_0=650 nm. For the ridge antenna we position the beam close to the end facet where the excitation probability of the in-plane dipole resonance is high [15]. We vary β from 0° to 170° in steps of 10° yielding 18 polarization-filtered angular patterns per dipole orientation. The two columns on the left of Fig. 4 show experimental angular emission patterns (CL emission intensity as function of zenithal angle θ and azimuthal angle ϕ) for β=0° and β=90° collected for all three orientations. The patterns are normalized to 1 to obtain similar contrast for each image. As expected, the collected pattern depends strongly on polarization and dipole orientation. Furthermore, the observed patterns deviate strongly from the patterns collected without polarizer [13, 15] (also see Fig. 2(a,b)). For the *x*-and *z*-dipole the emission is strong along the centerline of the mirror (from ϕ=0° to ϕ=180°), along the optical (*x*) axis) for β=0°, whereas for β=90° the centerline is dark and we see two transverse lobes. It is clear that these patterns are profoundly different from the calculated Fourier images for the microscope objective in Fig. 3.

In our setup we collect the CL emission using a reflective aluminum paraboloid mirror which has a polarization response that strongly differs from a microscope objective. Because of the paraboloidal shape the emission polarization direction after reflection is significantly altered. Furthermore, since the permittivity of aluminum has a non-negligible imaginary part in the visible spectral range, the emission polarization can become ellipsoidal after reflection for some incoming electric field orientations. Thus, in order to fully understand the experimental results we have to calculate what effect the mirror has on the polarization for each emission angle. To calculate the polarization-filtered angular pattern for a particular polarizer angle and dipole orientation we take the following approach. We define an emission vector $\hat{\mathbf{d}}$ which specifies the emission direction for a combination of θ and ϕ (Eq. 1(a)) which can be done by simply using spherical coordinates. For every emission direction, the electric field orientation $\hat{\mathbf{e}}$ for a dipole oriented along $\hat{\boldsymbol{\mu}}$ can be calculated, using the same asymptotic far-field expressions as used for Fig. 2. Note that the polarization direction is always perpendicular to the emission propagation
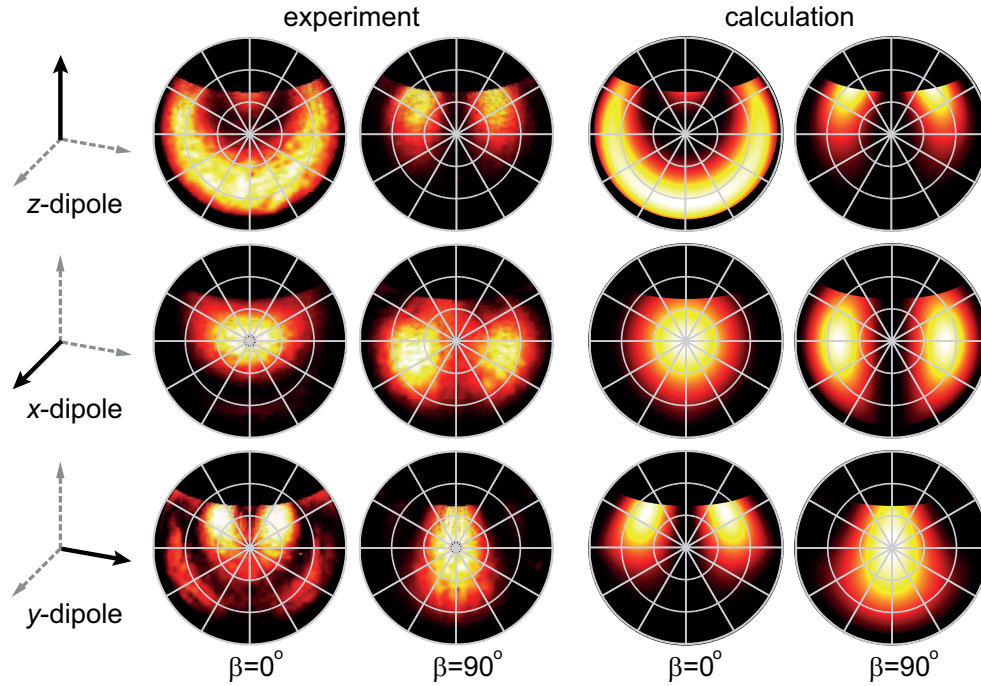
Fig. 4. Experimental (first two columns) and calculated (last two columns) angular cathodo-luminescence emission patterns for different dipole orientations and polarizer angles measured at $\lambda_0 = 650$ nm (30 keV electrons). The black area around $\phi = 0°$ is not collected by the mirror. The hole is located at $\theta = 0°$ in the center of the polar plot.

direction ($\hat{\mathbf{d}} \cdot \hat{\mathbf{e}} = 0$).

$$\hat{\mathbf{d}} = \begin{bmatrix} \sin\theta\cos\phi & \sin\theta\cos\phi & \cos\theta \end{bmatrix} \tag{1a}$$

$$\vec{\mathbf{c}} = \begin{bmatrix} ar^2 & r\cos\alpha & r\sin\alpha \end{bmatrix} \tag{1b}$$

To calculate the reflection properties we have to take into account the mirror geometry. The position of the paraboloid in cartesian space ($\vec{\mathbf{c}}$) can be parameterized terms of r and α where $r = (y^2 + z^2)^{1/2}$, $\alpha = \cos^{-1}(y/r)$ and a is the parabola coefficient which is 0.1 for our paraboloid. The surface normal of the paraboloid can be attained by taking the cross product of the α- and r-gradient of $\vec{\mathbf{c}}$.

$$\vec{\mathbf{n}} = \nabla_\alpha\vec{\mathbf{c}} \times \nabla_r\vec{\mathbf{c}} \tag{2}$$

Expressions for the gradients can simply be attained by symbolic differentiation of Eq. 1(b). To calculate the reflection at the mirror surface we need to calculate the Fresnel reflection coefficients for s-polarized (r_s) and p-polarized (r_p) light for different angles of incidence (AoI). Figure 5(a) shows $|r_s|^2$ and $|r_p|^2$ as function of the AoI for $\lambda_0 = 650$ nm [1]. The real and imaginary parts of the reflection coefficients are shown in the inset of (a). It is clear that the reflectivity for s-polarized light is always higher than for p-polarized light. The angle of incidence on the mirror for a light ray emitted in a direction $\hat{\mathbf{d}}$ is given by AoI $= \cos^{-1}(\hat{\mathbf{d}} \cdot \hat{\mathbf{n}})$. Figure 5(b) shows the AoI for all combinations of θ and ϕ. In some parts of the mirror the light reflects under quite a grazing angle (up to 63°). From Figs. 5(a,b) we can calculate r_s^2 and r_p^2 for
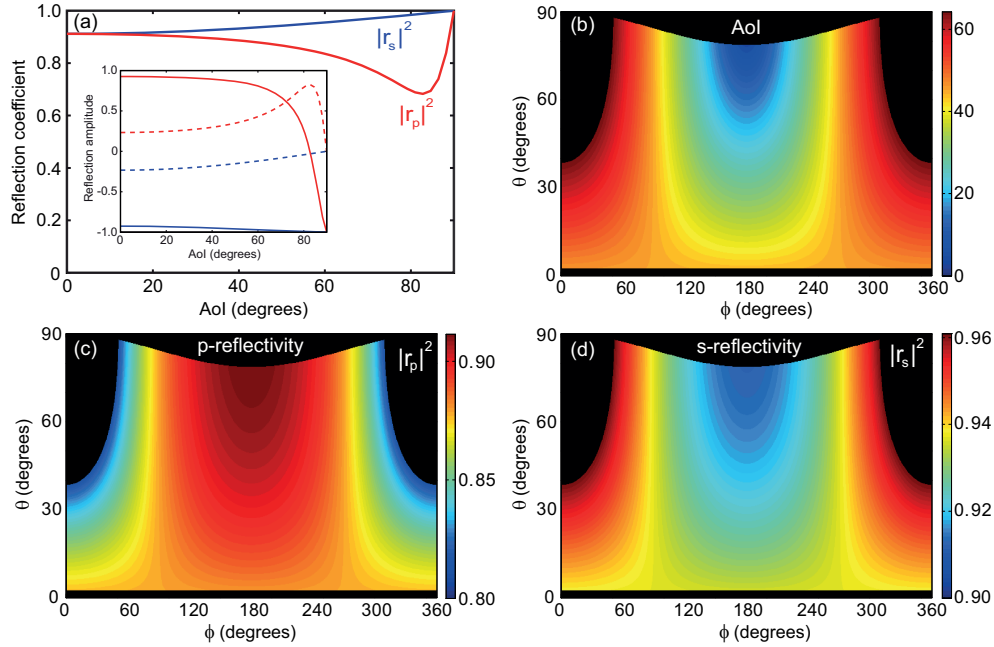
Fig. 5. (a) Reflectivity as function of angle of incidence (AoI) for an aluminum surface at $\lambda_0 = 650$ nm calculated for s-and p-polarized light. The inset shows the real (solid curves) and imaginary (dashed curves) parts of the Fresnel reflection coefficients for s-and p-polarized light. (b) Angle of incidence on the mirror surface for all emission angles θ and ϕ collected by the mirror. Angles that are not collected are colored black. (c) Reflectivity of the mirror for p-polarized light and (d) s-polarized light.

each emission direction (Figs. 5(c,d). The reflectivity is always higher than 0.8 for all collected emission angles and incoming polarizations.

By definition the s-polarization direction $\hat{\mathbf{s}}$ is given by $\hat{\mathbf{n}} \times \hat{\mathbf{d}}$ and the p-polarization direction $\hat{\mathbf{p}}$ is given by $\hat{\mathbf{d}} \times \hat{\mathbf{s}}$. Now we can decompose the incoming polarization into a p-polarized and s-polarized part by projecting $\hat{\mathbf{e}}$ onto $\hat{\mathbf{p}}$ and $\hat{\mathbf{s}}$. By multiplying the p-and s-components of the field with the appropriate Fresnel coefficients (see Fig. 5) we can calculate the electric field orientations after reflection. Note that we have to correct for the fact that the p-component of the field changes direction after reflection from the mirror in order to maintain the orthogonality with propagation direction. Since the paraboloid converts the light from a point source into a plane wave traveling along the x-direction the electric field only has y-and z-components after reflection. To find the electric field after the polarizer we have to multiply the field components with the Jones matrix for a linear polarizer.

$$\vec{\mathbf{E}}_{out} = \begin{bmatrix} E_y \\ E_z \end{bmatrix} \begin{bmatrix} \cos^2\beta & \sin\beta\cos\beta \\ \sin\beta\cos\beta & \sin^2\beta \end{bmatrix} \tag{3}$$

By multiplying $|\vec{\mathbf{E}}_{out}|^2$ with the characteristic angular intensity distribution for the dipole orientation under consideration (see Figs. 2(a,b) we can compare our calculations to the experiment and explain the observations.

The third and fourth column in Fig. 4 show the calculated polarization-filtered angular emission distributions. For the z-oriented dipole the calculation agrees very well with the data. For
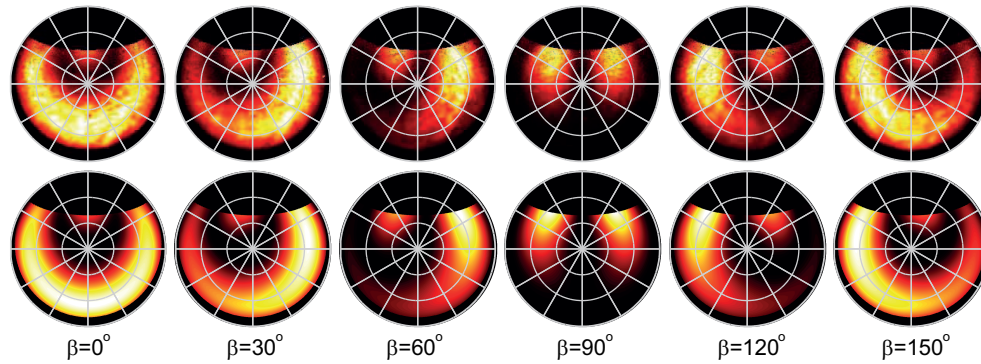
Fig. 6. Experimental (top row) and calculated (bottom row) polarization-filtered angular cathodoluminescence emission patterns for transition radiation measured for different polarizer angles at $\lambda_0 =$650 nm. Radiation patterns are shown for $\beta = 0°, 30°, 60°, 90°, 120°,$ and 150° respectively.

the line $\phi = 0 - 180°$ the emission is bright for $\beta = 0°$ and dark for $\beta = 90°$. The reflection of the radially polarized emission in the center of the mirror (along the x-axis at y=0) only has p-character and after reflection the electric field only has a z-component. For $\beta = 0°$ the field is fully transmitted whereas for 90° the field is blocked, explaining the bright and dark bands in the center. A similar explanation can be given for the x-dipole, where the reflection also only has p-character and the field after reflection is again oriented along z. The y-oriented dipole only has s-character in the center of the mirror (the field is aligned with y), and as a result we observe the opposite behavior: a dark band for $\beta = 0°$ and a bright band for $\beta = 90°$. The observed patterns are a convolution of the initial far-field intensity distribution (Fig. 2) with the emission polarization properties. The differences between the patterns for the different dipole orientations are due to both effects. It is clear that the calculation matches our experimental results better for the z-dipole than for the x-and y-dipole. We attribute this to the fact that the properties of the z-oriented transition dipole are very close to an analytical point dipole, whereas the antenna resonance has dipolar character but is not a pure point dipole due to the physical size and limited aspect ratio (2.5:1) of the antenna.

To illustrate that our approach works for other polarizer angles as well we show both the experimental and calculated patterns for the z-oriented dipole for $\beta = 0 - 150°$ in steps of 30° (Fig. 6). The gradual change of the angular pattern when rotating the polarizer is clearly visible in both the experiment and calculation, demonstrating the accuracy of our model.

4. Enhancing polarization contrast for cathodoluminescence spectroscopy

When using a microscope objective for detection of emission originating from an in-plane dipole above a gold substrate, the total intensity integrated over all collected angles (obtained from Fig. 3) is $\sim$30 times higher when the polarizer is aligned with the dipole axis than for the cross-polarized orientation. This means that when the collected optical scattering or fluorescence is sent to a spectrometer for spectral analysis one can clearly distinguish two dipole orientations by using a polarizer after light collection. Due to its azimuthally symmetric charge distribution there is no contrast for a z-dipole. As we have shown in the previous section, the mirror strongly affects the detected polarization. We can calculate the polarization contrast for our experimental setup by integrating the emission patterns shown in Fig. 4. The polarization contrast for our detection geometry is significantly lower than for the objective. Interestingly
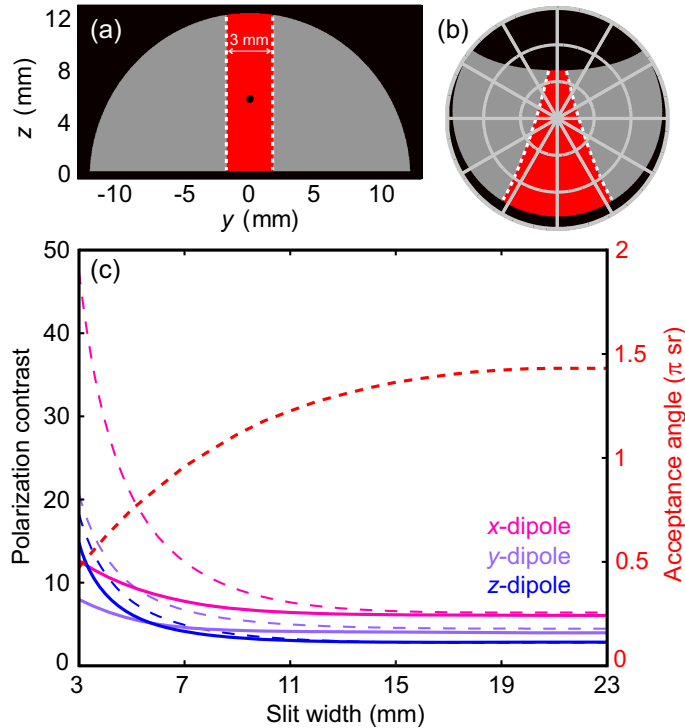
Fig. 7. (a) Front view of the mirror. The white dashed lines indicate the edge of a rectangular 3 mm slit placed in front of the mirror. The total width of the mirror is 23 mm. The part of the mirror from which light is collected is indicated by the red area and the parts that are blocked are shown in gray. The black dot in the center corresponds to the hole in the mirror (b) Polar plot showing which angles are blocked by the slit. (c) Experimental (solid curves) and calculated (dashed curves) polarization contrast for a z-, y-and x-oriented dipole as function of slit width. The slit was introduced numerically by appropriately clipping the experimental and calculated polarization-filtered angular patterns shown in Fig. 4. The red dashed line shows the amount of collected solid angle as function of slit width.

the contrast for x and y differ slightly which is due to the fact that the paraboloid mirror is not azimuthally symmetric in its response like an objective. This is also the reason why the contrast for z is not equal to zero like for the objective. The emission polarization is distorted less in the center of the mirror so by using a slit we can greatly enhance the polarization contrast in CL-spectroscopy. This approach has been employed previously to probe the polarization response of surface plasmon polariton (SPP) whispering gallery resonators [14]. Takeuchi *et al.* have taken a similar approach where they scan a pinhole over the mirror center to accurately determine the dispersion patterns of SPPs in two-dimensional metallic hole arrays [19]. Furthermore there are several groups that have performed polarization-sensitive CL-spectroscopy on semiconductor and metallic nanostructures where polarization measurements were performed without a slit [20-23].

Here we work out in detail what the effects are of introducing a slit in the beam path. Figure 7(a,b) shows what part of the mirror is blocked by a 3 mm slit (the total width of the mirror is 23 mm). Note that the rectangular slit gives an asymmetric shape in the polar plot due to the curvature of the paraboloid. In Fig. 7(c) we show how the polarization contrast depends

on the slit width for the three different dipole orientations both for theory (dashed curves) and experiment (solid curves). We have numerically introduced a slit by appropriately clipping both the experimental and calculated polarization-filtered patterns shown in Fig. 4 such that all the angles that would be blocked by the slit are set to zero. This was done for slit widths between 3 and 23 mm. For the z-dipole the experiment matches quite closely to the calculated curve and the polarization contrast is enhanced six times for a 3 mm wide slit. The small discrepancy between experiment and theory is mainly caused by imperfections in the detection system like the polarizer for instance, which does not fully block cross-polarized light. For the x-and y-dipole the experiment deviates substantially from the theoretical curve which we attribute to the fact that the ridge is not a perfect dipole emitter. Nevertheless the polarization contrast is enhanced by a factor of two for both dipole orientations (assuming a 3 mm slit) which is still useful for determining the dipole orientation in such structures. This technique could be employed in the future for probing the polarization properties for more complex structures where the orientation of the dipole moment is unknown *a priori*.

Although the polarization contrast is greatly enhanced by using a slit, the acceptance angle decreases (see red dashed curve in Fig. 7(c)) lowering the signal-to-noise (SNR) ratio. Furthermore the slit blocks certain emission angles and as a result it acts as a 'momentum filter'. Therefore one should be cautious in interpreting experimental results when dealing with highly directional antenna structures rather than omnidirectional dipolar emitters. Also it is difficult to distinguish between an x-or z-oriented dipole by the polarization response alone. The angular patterns are very different though (see Fig. 2) and can be used to differentiate between the two. Using this knowledge one can now pick the optimum slit width depending on the SNR, directionality of the structure under investigation, and the required polarization contrast. One could even envision using custom slit or pinhole shapes optimized for a particular angular region of interest.

5.   Emission polarization reconstruction

In section 3 we have shown how to calculate the polarization-filtered angular pattern if the emission polarization is known. We can also perform the reverse operation by extracting the emission polarization from the experimental data. For a particular emission angle we can plot the CL intensity as function of β. In Fig. 8(a) we have plotted the CL-intensity as function of β for $\phi = 180°$ and $\theta = 35°$ for all the three dipole orientations. As was explained in section 3, the intensity is maximum for the z/x-oriented dipole and minimum for the y-oriented dipole when $\beta = 0°$. For linearly polarized light the intensity varies as $\cos^2(\beta - \beta')$, where $\beta' = \tan^{-1}(E_y/E_z)$ represents the angle of the electric field with respect to the z-axis.

In some parts of the mirror the emission becomes slightly elliptical, as explained before. For elliptically polarized light the intensity does not go to zero. In that case the maximum value of the oscillation corresponds to the square of the semi-major axis of the polarization ellipse and the minimum corresponds to the square of the semi-minor axis. The maximum degree of ellipticity (DoE) is 0.22 where we define DoE as the ratio between the semi-minor and semi-major axis of the polarization ellipse. For most emission angles the offset in the intensity oscillation caused by this ellipticity is negligibly small and difficult to measure due to uncertainties in the measurement caused by noise and abberations/imperfections in the optics. Note that it is not possible to extract the complex field amplitudes from the shape of the polarization ellipse alone. To obtain all four independent Stokes parameters interferometric measurements or the addition of a circular polarizer in the beam path would be required [1]. In this reconstruction we will assume for simplicity that the collected emission is linearly polarized and neglect the phase pickup upon reflection from the mirror. We do divide the p-and s-components of the electric field by $|r_p|$ and $|r_s|$ respectively, to correct for the reflection losses from the mirror.
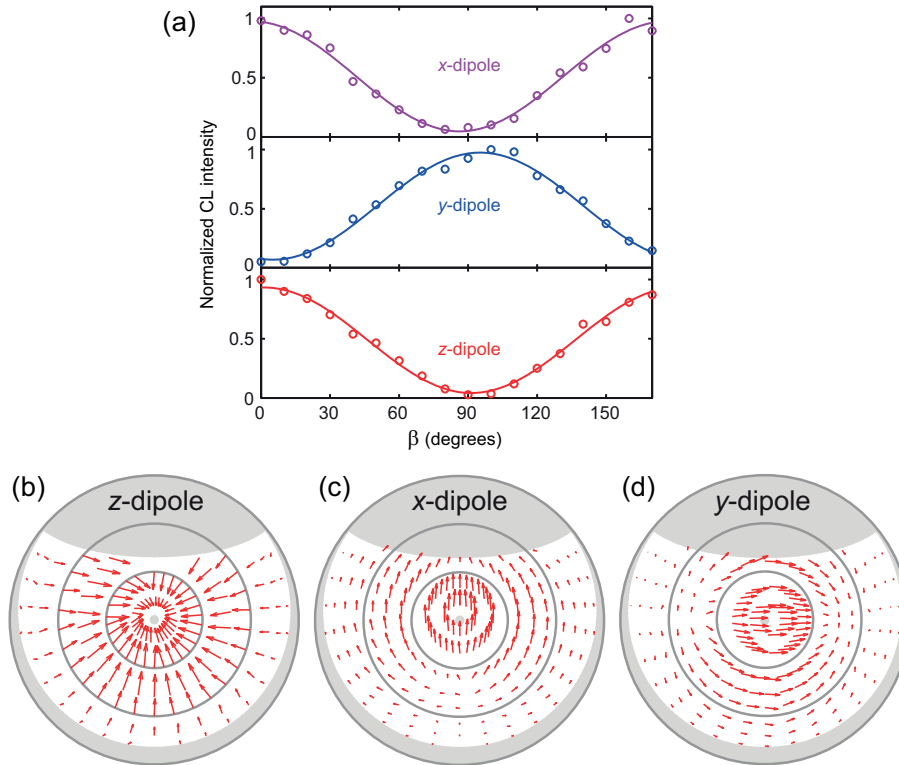
Fig. 8. (a) Normalized cathodoluminescence intensity as function of polarizer angle (β) for $\theta = 35°$ and $\phi = 180°$ for the three dipole orientations. The open circles represent the experimental data and the solid curves are the numerical fits. (b) Vector field plot showing the orientation of the electric field projected onto the xy-plane (top view of the vector field) for different emission angles (the gray concentric circles correspond to $\theta = 30°, 60°$, and $90°$ respectively) reconstructed from the experimental data for the z-dipole, (c) x-dipole, and (d) y-dipole. The light gray colored area corresponds to angles that are not collected by the mirror.

From the maximum value of the fitted $\cos^2$ function we can deduce the magnitude of the electric field and from the position of the maximum we can deduce the relative magnitude of E_z and E_y (the electric field orientation). Now we can do the inverse of what was done in section 3 by sending rays back into the mirror (in the negative x-direction) with the electric field orientation that was found from the fitting. This yields the amplitude and orientation of the electric field in 3D-space for each emission angle. It can be difficult to visualize vectors in 3D space, but to distinguish between the different dipole orientations we do not necessarily need E_z.

In Fig. 8(b-d) we show the emission polarization for z-, x-and y-oriented dipoles respectively. We only plot E_x and E_y as function of emission angle in a vector field plot where the direction of the arrows shows the orientation of the electric field in the xy-plane and the length of the arrows represents $(E_x^2+E_y^2)^{1/2}$. The base of the arrow corresponds to the emission angle in the polar plot. Note that in all plots the direction of the arrows can be rotated by $180°$ because the electric field changes sign every half optical cycle. In Fig. 8(b) the electric field vectors all are approximately pointing towards the center, thereby confirming that the emission from the

TR-dipole (z-dipole) is radially polarized as is expected from theory (see Fig. 2(c)) [17]. The electric field amplitude becomes smaller near $\theta = 0°$ as expected from the toroidal far-field pattern. However, the emission intensity should be maximum around $\theta = 60°$ which is not the case here [13]. This is due to the fact that the emission polarization has a large E_z component for the more grazing angles which is not visible in the plot (the plot is a top view of the vector field). In Figs. 8(c, d) the electric field is clearly aligned with the dipole moment (along x in Fig. 8(c) and along y in Fig. 8(d) respectively) and the patterns look similar to those of a point dipole [1, 2]. Thus, although this reconstruction neglects the phase change upon reflection we can clearly infer the orientation of the excited dipole moment without knowledge about the polarization direction of the source.

6. Conclusions

In conclusion, we have demonstrated a novel method to perform polarization-sensitive cathodoluminescence Fourier microscopy. As proof of principle we measured polarization-filtered angular emission patterns for three orthogonal dipolar sources and compared them with calculations where we assumed that we were driving a point dipole on the gold surface which was oriented along x, y, or z. The calculated polarization-filtered angular patterns show good agreement with experiments suggesting that the effect of the mirror on the polarization is well-captured by our model. Furthermore we calculate that introducing a slit in the beam path greatly enhances the polarization contrast which is useful for polarization-sensitive spatially-resolved mapping of the local density of optical states. Finally, we show that we can effectively reconstruct the emission polarization for each of the dipole orientations, assuming that the emission is linearly polarized and that the effect of the mirror on the relative phase between s-and p-components is negligible. The addition of polarization sensitivity makes the cathodoluminescence microscopy technique an even more powerful and versatile tool for probing the near-and far-field properties of nanophotonic structures. By including phase-sensitive detection in future experiments we could extract the full polarization state of the emission as function of wavelength, emission angle, and excitation position. This could lead to new insights in the polarization properties of more complex antenna and metamaterial designs.